Title
Potential Predictability of Southwest U.S. Rainfall: Role of Tropical and High-Latitude Variability

Journal
Journal of Climate, 35(6)

ISSN
0894-8755

Authors
Peings, Y
Lim, Y
Magnusdottir, G

Publication Date
2022-03-15

DOI
10.1175/jcli-d-21-0775.1

Peer reviewed

JGR Atmospheres

RESEARCH ARTICLE
10.1029/2021JD035028

The Role of Atmospheric Drivers in a Sudden Transition of California Precipitation in the 2012/13 Winter

Yuna Lim[1], **Yannick Peings**[1], **and Gudrun Magnusdottir**[1]

[1]Department of Earth System Science, University of California, Irvine, CA, USA

Key Points:

- California experienced a wet-to-dry transition during 2012/13 winter, but it was not predicted in the seasonal prediction models
- The wet conditions in November–December were driven by the tropical sea surface temperature (SST), which was missed in the seasonal prediction models
- The subseasonal prediction models that predicted the Madden-Julian Oscillation (MJO) were also able to predict the dry conditions in January

Supporting Information:

Supporting Information may be found in the online version of this article.

Correspondence to:

Y. Lim,
ylim5@uci.edu

Citation:

Lim, Y., Peings, Y., & Magnusdottir, G. (2021). The role of atmospheric drivers in a sudden transition of California precipitation in the 2012/13 winter. *Journal of Geophysical Research: Atmospheres*, *126*, e2021JD035028. https://doi.org/10.1029/2021JD035028

Received 8 APR 2021
Accepted 28 OCT 2021

Abstract California experienced a sharp transition from wet to historically dry conditions during the 2012/13 winter. Such transitions in the precipitation regime have strong consequences for water management, but predicting them at the seasonal time scale remains very challenging as little is known about what drives them. The 2012/13 winter was characterized by a neutral El Niño Southern Oscillation, strong Madden-Julian Oscillation (MJO) activity, and sudden stratospheric warming. This study examines the potential influence of these different drivers in atmospheric global climate model experiments with prescribed sea surface temperature (SST) and sea ice concentration and constrained tropical and/or Arctic variability. Our model results are compared to reforecasts from the North American Multi-Model Ensemble (NMME) and Subseasonal Experiment (SubX)/Subseasonal to Seasonal (S2S) projects to determine which important processes may have been missed by the seasonal prediction systems. Our simulations suggest that the tropical warm-west, cool-east SST anomaly played an active role in the wet conditions of November–December 2012 through a typical tropical-extratropical teleconnection. The tropical SST anomalies were not accurately predicted by the NMME models, and none of them predicted the wet anomalies in November–December. In contrast, the sudden transition toward dry conditions in January is found to be independent of tropical SST variability, and rather influenced by strong MJO activity over the western Pacific. The SubX/S2S models with a better MJO prediction tend to predict the dry conditions in January better. Our study highlights how intraseasonal processes superimpose on more persistent seasonal anomalies and induce regime shifts such as the wet-to-dry transition of the 2012/13 winter.

1. Introduction

The state of California is home to nearly 40 million people (U.S. Census Bureau, 2019) and is the leading United States (US) state in agriculture, accounting for over 13% of the country's total agricultural value (U.S. Department of Agriculture, 2020). Precipitation in the form of rain and high-elevation snow during the cold season (November–March) accounts for more than two-thirds of the annual precipitation (e.g., Cooper et al., 2018; Frankson et al., 2017; Swain et al., 2016). The precipitation that gets stored in mountain snowpack and engineered reservoirs during the cold season is a water resource for the entire water year (Guirguis et al., 2019; Knowles et al., 2006; Lund et al., 2018).

California (CA) experienced a historic drought over 2011–2017, with the 2011–2014 three-winter average precipitation for California recorded as the second driest over 100 years (Figure 1 of Seager et al., 2015). A strong El Niño in 2015/16 did not bring the expected precipitation over the state (e.g., S.-K. Lee et al., 2018; Paek et al., 2017; Singh et al., 2018). The peak of the drought over 2012/13–2015/16 was caused by the unusual multi-year persistence of ridging conditions in the eastern North Pacific, the so-called "Ridiculously Resilient Ridge" (Swain et al., 2014), that greatly interrupted the westward propagation of mid-latitude storms and atmospheric rivers over the west coast of the US (Swain et al., 2016). Several hypotheses have been made to explain the persistence of ridging conditions such as observed over 2012/13–2015/16: tropical Pacific sea surface temperature (SST) variability (Hartmann, 2015; M.-Y. Lee et al., 2015; Seager & Henderson, 2016; Seager et al., 2015; Watson et al., 2016), tropical western Pacific atmospheric variability (Watson et al., 2016), western North Pacific SST and convective activity (Wang et al., 2014), Arctic sea ice variability (Cohen et al., 2017; M.-Y. Lee et al., 2015; Swain et al., 2017), Arctic Oscillation (AO; Singh et al., 2018), or the wave patterns that are intrinsic to mid-latitude atmospheric dynamics (Teng & Branstator, 2017). Although these different drivers may all have played a role in driving the ridge, internal variability was likely a large factor, too (e.g., Seager et al., 2015; Watson et al., 2016).

Although ridging conditions prevailed during the California drought period, each year was characterized by specific climatic conditions that played a role in forcing the ridge, with different physical mechanisms. Using Atmospheric General Circulation Models (AGCMs) simulations, Seager et al. (2015) show the role of La Niña SST anomalies on the drought of 2011/12 winter, consistent with the ENSO-California precipitation relationship (e.g., Ropelewski & Halpert, 1986; Seager & Hoerling, 2014). The ENSO-CA rainfall teleconnection is more consistent under La Niña than El Niño conditions. The 2015/16 winter is a good example, since high-pressure anomalies prevailed over the southwest US, preventing much-needed atmospheric rivers and precipitation from hitting the region, despite one of the strongest El Niño on record (e.g., S.-K. Lee et al., 2018; Paek et al., 2017; Singh et al., 2018). For the 2012/13 and 2013/14 winters, Seager et al. (2015) found an influence for the warm-west, cool-east tropical Pacific SST pattern that was dominant, with neutral ENSO conditions. This is also supported by Hartmann (2015), M.-Y. Lee et al. (2015), Seager and Henderson (2016), Wang et al. (2014), and Watson et al. (2016) for the case of the 2013/14 winter. For the 2012/13 winter, the SST variability cannot fully explain the persistence of dry conditions (Seager & Henderson, 2016; Seager et al., 2015; Wang & Schubert, 2014).

Most studies have focused on the role of SST/sea ice boundary conditions, the main source of predictability for seasonal forecasting (Cohen et al., 2017; Hartmann, 2015; M.-Y. Lee et al., 2015; Seager & Henderson, 2016; Seager et al., 2015; Swain et al., 2017). However, the influence of tropical and high-latitude variability on the midlatitudes is not limited to SST/sea ice variability. Other atmospheric variabilities, such as the Madden-Julian oscillation (MJO; Madden & Julian, 1971) in the tropics, or polar stratosphere/annular mode variability in the Arctic, have the potential to drive the mid-latitude atmospheric dynamics through remote teleconnections. The MJO represents tropical convective activity, propagating eastward from the Indian Ocean to the central Pacific Ocean with a period of 30–60 days. The upper-level divergence associated with MJO convection is a source of Rossby waves that propagate into the extratropics (e.g., Hoskins & Karoly, 1981; Sardeshmukh & Hoskins, 1988). The MJO leads to a wave-induced trough or ridge in the eastern North Pacific depending on the phase of MJO activity, affecting weather in the western US, including California. For instance, MJO phases 4 and 5 with enhanced convection in the western Pacific promote dry conditions over California (Becker et al., 2011; Mo & Higgins, 1998). As mentioned in Wang et al. (2017), subseasonal variability, such as MJO, can become a predictable source of otherwise unpredictable atmospheric noise at the seasonal time scale. In addition to the tropical variability, Singh et al. (2018) showed that an accurate prediction of high-latitude atmospheric circulation anomalies in a seasonal forecast model experiment results in a successful simulation of CA rainfall difference between the 2015/16 and 2016/17 winters.

In the present study, we conduct a case study of the 2012/13 winter that we chose to focus on for the following reasons. The 2012/13 winter is an interesting case because California experienced a transition from relatively wet conditions in November/December to dry conditions for the rest of the season (black line in Figure 1a, Swain et al., 2014). The January to March (JFM) precipitation average in 2013 is the third driest JFM average over 1979–2019 (Figure 1c), while the 2012 October to December (OND) average is slightly above average (Figure 1b). According to Wang and Schubert (2014), the 2013 January–February average of precipitation is the driest over 1895–2014. Although the lack of rain in the 2012/13 winter was as pronounced as in the 2013/14 winter, the 2012/13 winter has been less studied than the 2013/14 and 2015/16 winters. Such wet-to-dry transitions in the middle of winter are particularly challenging for decision-makers who need to plan water usage for the rest of the rain season (Wang & Schubert, 2014). The seasonal prediction models failed to predict the wet-to-dry transition that occurred in January 2013. The CA precipitation forecast by each model from the North American Multi-Model Ensemble (NMME; Kirtman et al., 2014) is plotted in Figure 1a. Even at a 1.5-month lead time, the moderately wet conditions in November 2012 were poorly predicted by the models (colored lines in Figure 1a), and none of the models predicted the wet-to-dry transition. This is consistent with limited skill in predicting precipitation over the western US (e.g., Becker et al., 2020; Kumar & Chen, 2020; Slater et al., 2019), and it underscores the challenge of predicting regime shifts in CA precipitation months in advance. The upgrade or replacement of NMME models did not improve CA precipitation seasonal forecasting (Becker et al., 2020). Kumar and Chen (2020) point out that the low prediction skill is likely due to a low signal-to-noise ratio over California. The 2012/13 winter is also interesting because it was characterized by neutral ENSO conditions in the tropical Pacific, a strong MJO activity, and a negative phase of the AO associated with a sudden stratospheric warming (SSW;

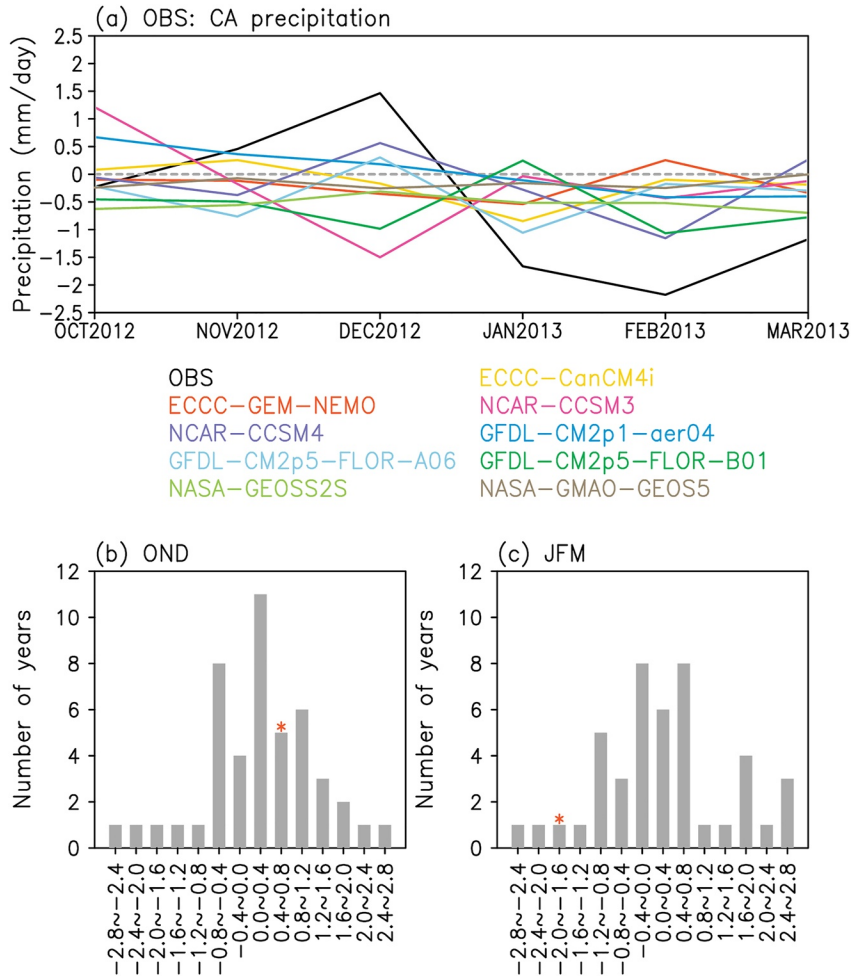

Figure 1. (a) Time series of California (CA) precipitation anomalies from October 2012 to March 2013. The black line denotes the observations, and each colored line refers to a North American Multi-Model Ensemble (NMME) model initialized in October. (b)–(c) Histograms of (b) October to December (OND)-mean and (c) January to March (JFM)-mean CA precipitation anomalies for 1979–2019. Red asterisks denote the OND 2012 and JFM 2013, respectively. The anomalies are obtained by subtracting the 1981–2010 climatology.

Baldwin et al., 2021) that occurred in early January 2013 (Xu & San Liang, 2017). Therefore, this winter is an interesting case to examine the role of MJO and high-latitude variability on CA rainfall and its wet-to-dry transition.

In this study, we explore the potential role of tropical and high-latitude variability using a set of regular AMIP simulations and "AMIP-plus" simulations that are partially constrained to observations within certain regions of the model domain. This allows us to assess potential predictability associated with not only SST/sea ice concentration (SIC) variability, but also "full" tropical and high-latitude variability. A nudging technique is used to impose tropical and high-latitude variability in an AGCM. This is an approach similar to Watson et al. (2016), who compared the influence of tropical western Pacific SST with the influence of tropical western Pacific atmospheric variability, for 2013/14 winter, by relaxing the atmosphere in the tropical western Pacific.

Using a set of AMIP/AMIP-plus experiments, we aim to reveal drivers of the 2012/13 winter variability and in particular of the wet-to-dry shift in rainfall conditions. We put our results in perspective with seasonal forecasts from the NMME and subseasonal forecasts from the Subseasonal Experiment (SubX; Pegion et al., 2019) and Subseasonal to Seasonal (S2S; Vitart et al., 2017) prediction projects to highlight potential reasons for the failure of S2S prediction models in predicting seasonal CA rainfall in 2012/13. Although we

Table 1
Descriptions of AMIP and AMIP-Plus Experiments Used in This Study

Experiment name	Descriptions
AMIP	37-year experiment prescribed observed SST and SIC over the 1980–2016 period
AMIP_TROP	Same as AMIP experiment but with additionally nudged tropical variability (30°S–22°N, <150 hPa)
AMIP_TRHL	Same as AMIP experiment but with additionally nudged tropical (30°S–22°N, <150 hPa) and high-latitude variability (>65°N, <300 hPa)

analyze a single year in this study, our objective is to reveal potential physical mechanisms and model limitations that may be of more general interest for seasonal forecasting. The plan of the study is as follows. The model experimental design is described in Section 2, along with the seasonal and subseasonal forecast data that we used. Section 3 explores physical mechanisms for the 2012/13 wet-to-dry transition using the AMIP and AMIP-plus experiments. In Section 4, we highlight potential reasons for the failure of seasonal forecast systems to predict the transition. Section 5 provides a summary and discussion of the results.

2. Data and Model

2.1. Observational Data

Daily and monthly averaged 200, 500, and 1000-hPa geopotential height for the 1980–2016 period is obtained from the Modern-Era Retrospective analysis for Research and Applications, Version 2 (MERRA-2; Gelaro et al., 2017). We use this field from reanalysis data to diagnose the atmospheric circulation during the 2012/13 winter. The Climate Prediction Center (CPC) US Unified Precipitation data are provided by the NOAA/OAR/ESRL PSL and are used to characterize the CA precipitation. We also use the precipitation data from the Global Precipitation Climatology Project (Adler et al., 2003) to ensure results are robust in another data set. We found similar results when using GPCP and CPC, so only results using the CPC data are shown in the study. The Hadley Center monthly SST data set version 1 (HadISST; Rayner et al., 2003) is used to characterize SST variability. Finally, the National Oceanic and Atmospheric Administration (NOAA) daily Outgoing Longwave Radiation (OLR; Liebmann & Smith, 1996) data are used to diagnose tropical convective activity. For all fields, daily and monthly anomalies are calculated by removing the 1981–2010 climatology.

2.2. Model and Experimental Design

All AGCM experiments are performed using the Specified Chemistry Whole Atmosphere Community Climate Model, version 4 (SC-WACCM4; Smith et al., 2014). SC-WACCM4 is a high-top atmospheric model with 66 vertical levels up to 5.1×10^{-6} hPa. The horizontal resolution is 1.9° latitude and 2.5° longitude. Table 1 describes the three main AGCM experiments used in this study. Each experiment consists of 10 ensemble members that span the 1980–2016 period. Each ensemble is generated by adding a tiny temperature perturbation in the atmospheric initial conditions. They include observed external forcings (greenhouse gases, aerosols, and solar radiation) and a prescribed Quasi-Biennial Oscillation (QBO) that follows observed radiosonde data over 1980–2016. Greenhouse gas and aerosol concentrations are set to the fixed values from the year 2000. Here is a description of the experiments:

1. **AMIP** is a traditional AMIP experiment with time-varying SST and SIC. Monthly mean observed SST/SIC used as boundary conditions come from Hurrell et al. (2008). AMIP highlights the influence of observed SST/SIC anomalies on climate variability of the 1980–2016 period.

Two additional perturbation experiments (i.e., AMIP-plus experiments) are conducted to examine other potential drivers from the tropics and from the high latitudes.

2. **AMIP_TROP** is an experiment in which tropical variability is controlled through relaxation (or nudging) of zonal wind, meridional wind, temperature, and surface pressure, at every time step of the model. Between 30°S and 22°N, these fields are nudged toward a target state that represents 3-hourly anomalies of the MERRA-2 reanalyses. Since reanalyses cannot be directly nudged in the model (that would

create inconsistencies due to different mean states in the model and the real world), the daily model climatology is interpolated into 3-hourly data, and then MERRA-2 anomalies are superimposed on the model climatology. The nudging is imposed from the surface up to 150 hPa to efficiently constrain the tropical troposphere toward observed variability. By doing so, we prescribe modes of tropical variability over various time scales, most notably the MJO. Its impact on mid-latitudes, more specifically on CA precipitation, can then be assessed.

3. **AMIP_TRHL** includes additional nudging of tropospheric high-latitude variability, north of 65°N, from the surface up to 300 hPa. It allows us to explore the potential role of high-latitude processes on the 2012/13 CA rainfall variability, including the persistence of negative AO conditions during the 2012/13 winter.

We also performed AMIP_HL experiments (Table S1), similar to AMIP_TRHL but with nudging in the high-latitudes only. It is briefly mentioned in the paper to discuss the impact of high-latitude variability in isolation. Ensemble averages of these experiments partly remove the influence of internal variability and isolate the forced response to the imposed forcing. Like for observations, the daily and monthly anomalies are defined by subtracting the 1981–2010 climatology.

Figure 2a shows the spatial distribution of the mean observed SST anomaly in December–February (DJF) 2012/13. Using the AMIP experiment, we can explore the role of the observed global SST/SIC anomalies on the atmospheric circulation during the 2012/13 winter (Figure 2b). The largest SST anomalies were found in the North Pacific, with warm anomalies in the central North Pacific and cold anomalies to the west and east. Tropical SST anomalies were overall weak, with moderate warm anomalies in the South China Sea and the eastern Indian Ocean and moderate cool anomalies in the eastern tropical Pacific (they were too weak to be classified as La Niña). These weak tropical SST anomalies were suggested as drivers of dry/ridge conditions over the western US in 2012/13 winter (Seager et al., 2015). Slight differences between observed SST and AMIP skin temperature (Figures 2a and 2b) are due to the use of a different SST data set in the AMIP runs, that is, the merged product of HadISST and NOAA weekly optimum interpolation SST analysis of Hurrell et al. (2008).

The observed MJO activity during the 2012/13 winter is shown in Figure 2c, using a Hovmöller diagram of equatorially (15°S–15°N) averaged and 20–100 days filtered NOAA OLR and MERRA-2 850-hPa zonal wind anomalies. Strong MJO activity is visible from the end of December to the end of February, consistent with about 1.5 of the DJF-mean OLR-based MJO index (OMI; Kiladis et al., 2014). The enhanced convection anomalies develop in the Indian Ocean and propagate in the central Pacific to the end of January, and redevelop in the Indian Ocean (Figure 2c). The lower level westerly (easterly) wind to the west (east) of enhanced convection shows a systematic change with the convective activity. Overall, the MJO activity is efficiently prescribed when tropical variability is nudged in the model (Figure 2d). The simulated OLR is not exactly equal to the observed OLR because OLR is defined at the top of the atmosphere, outside of the nudging domain. However, the OLR and MJO variability is very close to observations, so that its related teleconnection and effects on CA precipitation can be examined in the AMIP-plus simulations (Figure 2d). Note that the MJO is not well simulated by the model so it is almost absent in AMIP (not shown).

AMIP_TRHL is forced in the tropics as well as in the high-latitude Arctic troposphere (65°–90°N, below 300 hPa; blue circle in Figure 2f). This experiment allows us to isolate the potential influence of high-latitude variability on the wet-to-dry transition. A negative AO index persisted from October 2012 to March 2013 with −1.36 of average value (estimated from the CPC monthly AO index). As shown in Figures 2e and 2f, the anomalous anticyclonic circulation of the negative AO in high-latitudes is efficiently prescribed in AMIP_TRHL. Of course, the AO is not strictly a high-latitude process, and it is the result of eddy-mean flow interaction in midlatitudes. However, by nudging the high-latitudes, we constrain the location of the midlatitude flow and jet streams on their poleward flank, that is, we partially prescribe AO variability in the models. The potential influence of other high-latitude processes, particularly the downward effect of SSW in the Arctic troposphere, is likely included by nudging the Arctic troposphere to reanalysis.

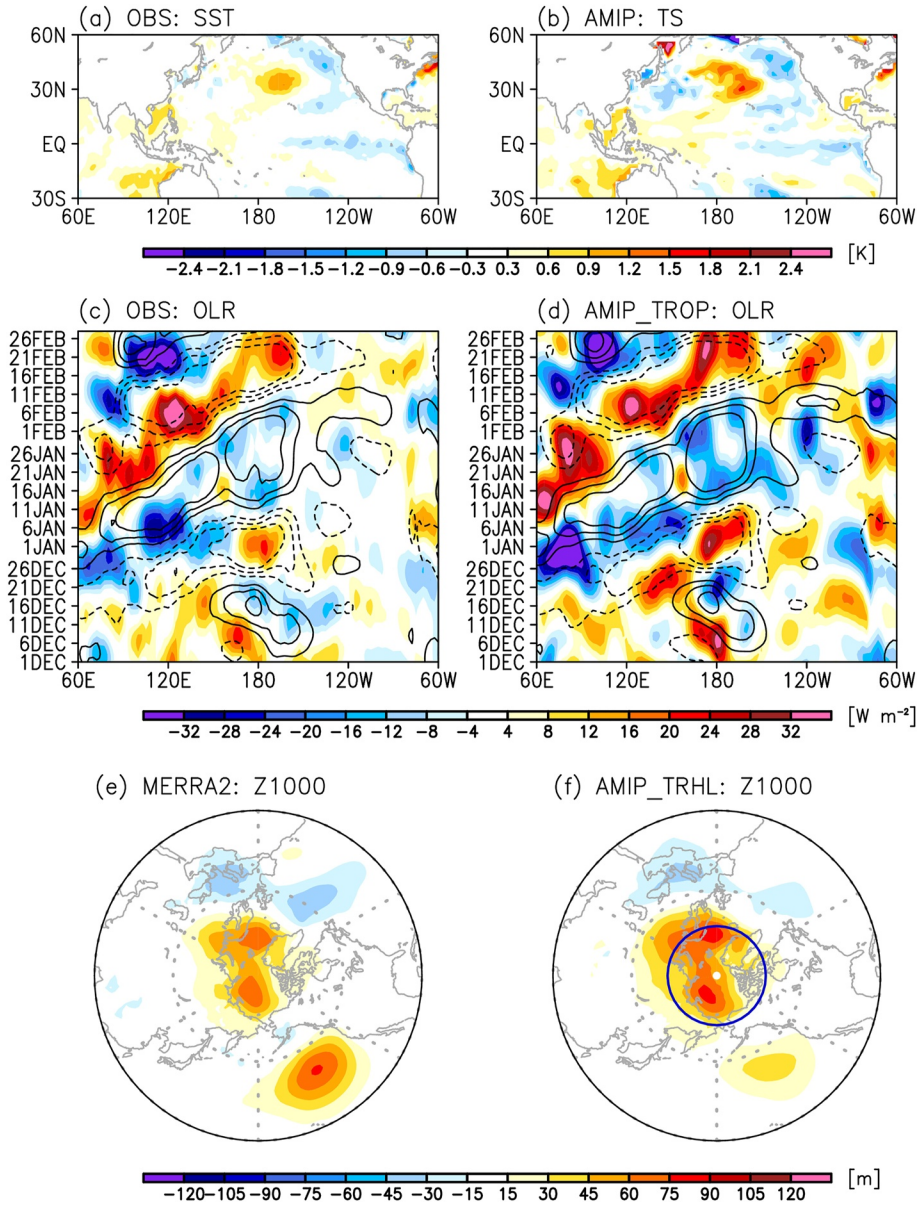

Figure 2. (a) Sea surface temperature (SST) anomalies averaged over December–February (DJF) of 2012/13 in observations. (b) Same as (a) but for skin temperature (TS) anomalies in AMIP. (c and d) Hovmöller diagrams of 20–100 days filtered Outgoing Longwave Radiation (OLR) anomalies (shaded) and 850-hPa zonal wind anomalies (contoured at ±3, ±2, and ±1 m s^{-1}) from December 1 to February 28 in (c) observations and (d) AMIP_TROP. The OLR and zonal wind anomalies averaged over the tropics (15°S–15°N) are shown. (e and f) 1000-hPa geopotential height (Z1000) anomalies averaged over DJF of 2012/13 in (e) Modern-Era Retrospective Analysis for Research and Applications, Version 2 (MERRA-2) and (f) AMIP_TRHL; the blue circle at 65°N denotes the edge of the nudging domain in AMIP_TRHL.

2.3. Seasonal Prediction Models

Seasonal forecasts from the North America Multi-Model Ensemble (NMME; Kirtman et al., 2014) are used to investigate how the 2012/13 wet-to-dry transition was predicted and why models failed to predict it. Table 2 presents the nine NMME models used in this study. The selection of models is made based on the availability of the SST, 200-hPa geopotential height (Z200), and precipitation fields in the International Research Institute (IRI) archive for the NMME data set. The NMME model forecasts analyzed here are a combination of both hindcasts and real-time predictions. The forecasts are initialized every month, we use the forecasts

Table 2
Descriptions of the North American Multi-Model Ensemble (NMME) Models Used in This Study

Model	Forecast period	Forecast length (month)	Ensemble size	Model resolution
ECCC-CanCM4i	1981-present	0.5–11.5	10	T63L31
ECCC-GEM-NEMO	1981-present	0.5–11.5	10	about 1.4° × 1.4° L79
NCAR-CCSM3	1982–2018	0.5–11.5	6	T85L26
NCAR-CCSM4	1982-present	0.5–11.5	10	0.9° × 1.25° L26
GFDL-CM2p1-aer04	1982-present	0.5–11.5	10	2° × 2.5° L24
GFDL-CM2p5-FLOR-A06	1980-present	0.5–11.5	12	C18L32
GFDL-CM2p5-FLOR-B01	1980-present	0.5–11.5	12	C18L32
NASA-GEOSS2S	1981-present	0.5–8.5	4	0.5° × 0.5° L72
NASA-GMAO-GEOS5	1981–2018	0.5–8.5	11	1° × 1.25° L72

initialized in October and November to verify whether the rainfall transition of the 2012/13 winter was predicted by the models. The NMME models have at least 8.5 months of forecast lead time (in the case of the two NASA models), and up to 11.5 months forecast lead time. The forecast ensemble means and monthly means are analyzed in this study. The monthly climatology of each model is calculated by averaging all the forecasts initialized on a given month over the common period of 1982–2010. As the monthly climatology is subtracted from the raw data to compute the anomalies, the model bias is removed. This is an important step to improve the skill of the NMME models (Barnston et al., 2015).

2.4. Subseasonal Prediction Models

To examine the impact of the subseasonal variability, reforecasts from the SubX (Pegion et al., 2019) and S2S prediction (Vitart et al., 2017) projects are used, instead of the NMME models. The daily data of NMME models are mostly provided until 2012, and therefore the analysis for 2012/13 winter is not available. Table 3 provides information about the 12 subseasonal prediction models considered in this study (two versions of NCAR-CESM1 with differing model levels in the stratosphere, five SubX, and five S2S models), including the initialization interval, ensemble size, horizontal resolution, and reforecast period. The model selection is based on the availability of data for 2012/13 winter. Vitart et al. (2017) and Pegion et al. (2019) provide more information on each S2S and SubX model's configurations, respectively. All models include a minimum of one forecast per week, with a reforecast length between 32 and 62 days (Table 3). The climatology

Table 3
Descriptions of the Subseasonal Experiment (SubX) and Subseasonal to Seasonal (S2S) Models Used in This Study

Model	Reforecast period	Reforecast frequency	Reforecast length (days)	Ensemble size	Model resolution
NCAR-30LCESM1	1999–2015	1/week	45	10	0.9° × 1.25° L30
NCAR-46LCESM1	1999–2015	1/week	45	10	0.9° × 1.25° L46
NASA-GEOS	1999–2015	Every 5 days	45	4	0.5° × 0.5° L72
RSMAS-CCSM4	1999–2016	1/week	45	3	0.9° × 1.25° L26
ESRL-FIM	1999–2016	1/week	32	4	About 60 km L64
Navy-ESPC	1999–2016	4/week	45	4	T359 L50
NCEP-GEFS	1999–2016	1/week	35	11	T574/382 L64
BoM-POAMA	1981–2013	6/month	62	33	T47 L17
CMA-BCC	2004–2018	2/week	60	4	T266 L56
ECMWF-Cy41r1	1996–2013	2/week	46	11	T639/319 L91
ECCC-GEPS	1998–2017	1/week	32	4	0.35° × 0.35° L45
UKMO-GloSea5	1993–2015	1/week	60	3	N216 L85

of the SubX and the two CESM1 models, which is computed for 1999–2015 and provided in the IRI archive, is used to calculate the anomalies. Since the climatology of the S2S models is not provided, it is computed by averaging the reforecasts initialized on the same date over the entire period of analysis, in line with previous studies (e.g., Lim et al., 2018; Vitart et al., 2017). The ensemble size of the models ranges from 3 (i.e., RSMAS-CCSM4, UKMO-GloSea5) to 33 (i.e., BoM-POAMA) ensemble members. In this study, the analyses are based on the ensemble mean of each model's reforecasts.

3. Results From the AMIP and AMIP-Plus Experiments

To reveal potential mechanisms for the wet-to-dry transition of the 2012/13 winter, this section examines the precipitation and circulation response to the imposed forcings in the three AMIP experiments (Table 1). Figure 3 shows the 500-hPa geopotential height (Z500) and precipitation anomalies in MERRA-2 and the three model experiments in December 2012, when a trough was present in the eastern North Pacific (Figure 3a) that brought precipitation over California (Figure 3b). Note that the trough was already present in November (Figure S1a). Figure 4 shows January anomalies, when persisting ridging conditions in the eastern North Pacific (Figure 4a) prevented atmospheric rivers from bringing precipitation over the southwest US (Figure 4b). Figure 5 summarizes the evolution of monthly mean CA precipitation anomalies in observations (in red) and in the model experiments. The eastern North Pacific (ENP; 150°–110°W, 30°–55°N) Z500, which is a proxy for the CA precipitation, is also examined in Figure 5b. The correlation between DJF-mean CA precipitation and DJF-mean ENP Z500 in MERRA-2 is −0.74 over 1979–2017. In MERRA-2, the Z500 anomalies over the North Pacific change from a trough in November–December to a ridge in January–March (Figures 3a, 4a, and 5b). This is consistent with the wet-to-dry transition shown in Figure 1a and also visible in Figure 5a.

In December, a tropical-extratropical teleconnection pattern is present in the North Pacific with a trough/ridge/trough wave train of Z500 anomalies from East Asia to eastern North Pacific/western North America (Figure 3a). This pattern has a barotropic structure, which is visible in Z200 anomalies (not shown). Let's now examine the model experiments. AMIP, AMIP_TROP, and AMIP_TRHL simulate a certain degree of the observed trough/ridge/trough wave train that propagates over the North Pacific in December (Figures 3c, 3e, and 3g). In particular, the North Pacific ridge and the ENP trough appear in all three simulations and accompany the anomalously wet conditions in the western US, even though their location and amplitude are slightly different between the simulations (Figures 3d, 3f, and 3h).

To quantitatively measure the agreement between model experiments and observations, the spatial correlations of Z500 anomalies between MERRA-2 and each experiment are given in Table 4. The spatial correlation is calculated over the North Pacific (120°E–120°W, 30°–55°N) to encompass the tropical-extratropical wave train, outside the nudging area (Table 1). In December, the spatial correlations in AMIP, AMIP_TROP, and AMIP_TRHL are very similar, with respective values of 0.81, 0.79, and 0.83. The difference in ENP through anomalies between AMIP_TROP, AMIP_TRHL, and AMIP is not statistically significant (Figure S4). This result reveals that AMIP already does a good job in reproducing the observed anomalies (Figures 3c and 3d, Table 4), indicating that SST variability played a role in the ENP trough that brought precipitation over California in November–December 2012. This further suggests that November–December 2012 was a window of opportunity for NMME seasonal forecasts that mostly rely on SST variability, unlike subseasonal forecasts. Of course, this is provided that SST anomalies are well predicted in the NMME models, a question we will discuss in Section 4.1.

A logical question to ask is which SST anomalies were most important in driving the wave train and promoting the wave train pattern. This is difficult to answer without further dedicated experiments, but it is likely that the tropical SST pattern of warm SST anomalies in the South China Sea (above 0.6 K) and weak cool anomalies in the eastern Pacific (Figure 2a) were influential (Barsugli & Sardeshmukh, 2002; Li & Forest, 2014; Newman & Sardeshmukh, 1998). The midlatitude anomalies (cold/warm/cold anomalies collocated with the trough/ridge/trough wave train in the North Pacific) were likely driven by the wave train pattern rather than the other way around (Lau & Nath, 1994).

Unlike for November–December, little of the midlatitude wave train in January–March 2013 can be explained by SST variability (Figures 4, S2, and S3). AMIP captures the dry/ridge anomalies in January–March

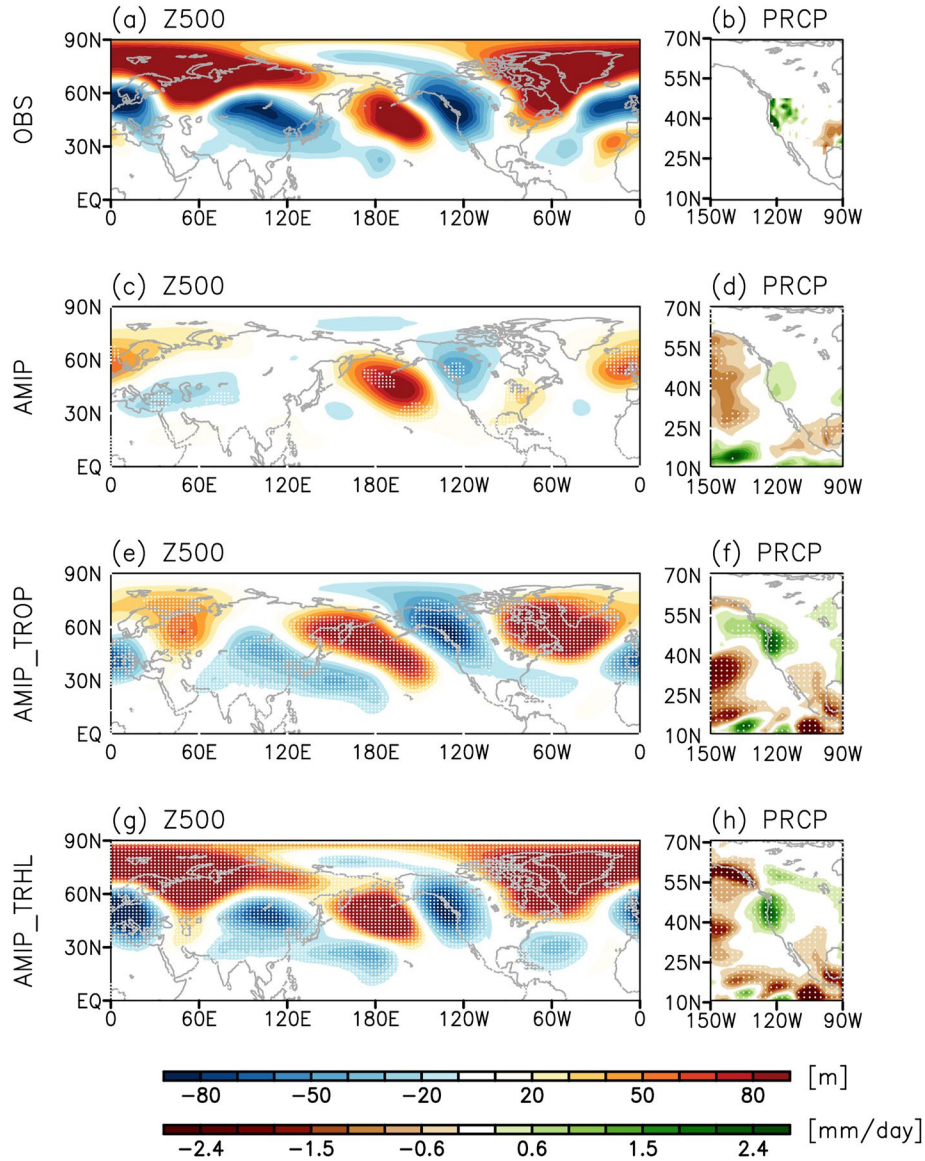

Figure 3. (a) 500-hPa geopotential height anomalies from Modern-Era Retrospective Analysis for Research and Applications, Version 2 (MERRA-2) reanalysis and (b) precipitation anomalies from CPC in December 2012. (c and d) Same with (a and b) but in AMIP simulation. Different from (a and b), the statistically significant values at the 95% confidence level are marked with white closed circles in (c and d). (e and f) Same as (c and d) but in AMIP_TROP simulation. (g and h) Same as (c and d) but in AMIP_TRHL simulation.

2013, but with weak amplitude and a large ensemble spread (see also yellow bars in Figure 5). This is consistent with Figure 2e of Wang and Schubert (2014) also found dry conditions in their simulations with a large ensemble spread. Although AMIP exhibits a weak ridge anomaly over the eastern North Pacific and a weak dry anomaly over the western US in January, the ridge is shifted westward compared to MERRA-2 reanalysis (Figures 4a and 4c). The low spatial correlation ($R = 0.44$ in Table 4) supports that the observed circulation pattern is not well represented in AMIP. In February and March, the performance further degrades in AMIP, and the spatial correlation drops to −0.03 (Table 4). In contrast, AMIP_TROP captures the amplitude and position of the ENP ridge (Figure 4e; see also Figures S2e and S3e) and associated precipitation deficit (Figures 4f, S2f, and S3f), highlighting a role for tropical variability in the wet/trough to dry/ridge transition. The ENP ridge in AMIP_TROP is significantly different and larger than that in AMIP (Figure S4b). The spatial distribution of Z500 anomalies over the North Pacific becomes closer to MERRA-2

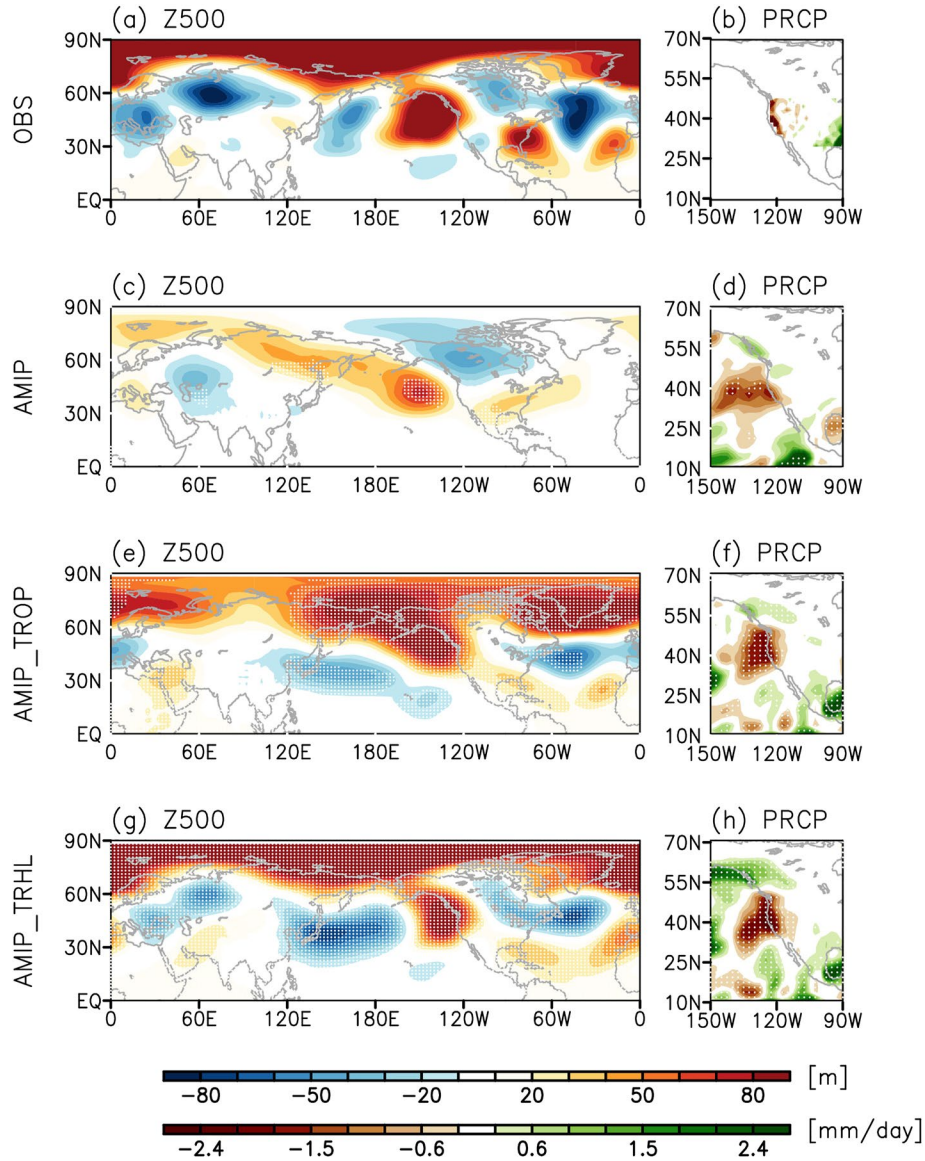

Figure 4. Same as Figure 3 but for January 2013.

($R = 0.70$ in Table 4). A large positive anomaly extends from the Bering Sea to the eastern North Pacific, and a higher Z500 is found in the Arctic (Figure 4e). The structure and amplitude of the ridge are more accurately represented in AMIP_TRHL (Figures 4g and 5b). It looks like a cut-off high being stretched out from the Arctic. However, the ridge is not significantly different from that in AMIP_TROP, indicating that the high-latitude variability only has a secondary role in the transition (Figure S4d). When only high-latitude variability is nudged in AMIP_HL, the ENP ridge is not of larger amplitude and is shifted northward than that in AMIP_TROP (Figures S4f and S5c). The cyclonic circulation anomaly over the North Pacific transports water vapor over California, promoting weak wet conditions (Figure S5d). Altogether, these findings suggest that tropical SST and atmospheric variability played a significant role in the wet-to-dry transition of CA precipitation of the 2012/13 winter. High-latitude atmospheric variability by itself does not bring any predictability, but when coupled with a good representation of the tropics, it refines the shape of the tropical-extratropical wave trains and provides some additional skill. Interestingly, it also generally reduces the spread in the model response, an important factor for a successful forecast.

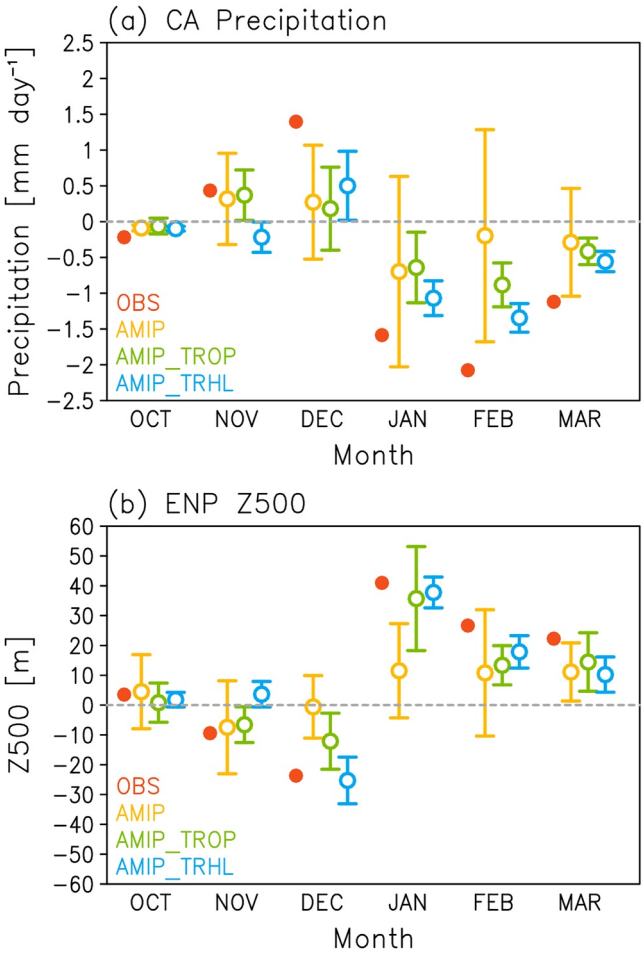

Figure 5. The observed and modeled monthly mean (a) California (CA) precipitation and (b) eastern North Pacific (ENP; 150°–110°W, 30°–55°N) Z500 anomalies from October 2012 to March 2013. The red closed circle indicates observations. The yellow, green, and blue open circles are the ensemble mean values in each month from AMIP, AMIP_TROP, and AMIP_TRHL, respectively. The error bar indicates a 95% confidence interval for each ensemble mean value.

Table 4
Spatial Correlation of Z500 Anomalies Over the North Pacific (120°E–120°W, 30°–55°N) of the AMIP and AMIP-plus Experiments With Modern-Era Retrospective Analysis for Research and Applications, Version 2 (MERRA-2) in Each Month

Experiment name	2012.11	2012.12	2013.01	2013.02	2013.03
AMIP	0.91	0.81	0.44	0.40	−0.03
AMIP_TROP	0.94	0.79	0.70	0.10	0.43
AMIP_TRHL	0.79	0.83	0.80	0.80	0.86

We further explore the influence of the tropics by investigating the impact of the MJO on the dry/ridge conditions of January 2013 in AMIP_TROP. As mentioned in Section 2, the MJO was particularly active during the 2012/13 winter (Figure 2c). Under phases 4 and 5 of the MJO, dry conditions tend to dominate over California due to MJO teleconnection in the extratropics (Becker et al., 2011; Mo & Higgins, 1998). Based on the OMI, strong MJO phases 4 and 5 dominated in early January, associated with enhanced convection in the western Pacific (Figure 2c). Tropical convection induces upper-level divergence anomalies that drive Rossby wave propagation from the tropics to the extratropics (e.g., Hoskins & Karoly, 1981; Sardeshmukh & Hoskins, 1988). Figure 6 reveals the large-scale atmospheric anomalies that may have resulted from the MJO-related tropical perturbations in January 2013. It shows the observed and modeled Z200 and OLR anomalies, averaged from January 2 to January 14, when the OMI was in MJO phases 4 and 5. The variables are filtered using a 20–100-day bandpass filter to isolate MJO-related variability. To account for the timing of Rossby wave propagation from the tropics into the extratropics, the 5-day and 10-day time-lagged responses of Z200 are also shown in Figures 6c–6f. The averaged value for January 7–19 corresponds to the 5-day lagged response, and the 10-day lagged response corresponds to the January 12–24 average.

AMIP_TROP exhibits a pattern of MJO teleconnection that closely resembles observations. At lag 0, strong enhanced convection due to MJO phases 4 and 5 is visible in the western Pacific, both in observations and AMIP_TROP (dashed green contours in Figures 6a and 6b). It is associated with a Rossby wave train that propagates in the North Pacific and North America, with a smaller amplitude in AMIP_TROP but a similar spatial structure. At lag 5 and 10 days, the western North Pacific trough weakens, and a ridge emerges and intensifies over the eastern North Pacific (Figures 6d and 6f), similar to MERRA-2 (Figures 6c and 6e). The ENP ridge is statistically significant in AMIP_TROP and AMIP_TRHL, whereas it is absent in AMIP (Figure S6). The daily time series of ENP Z500 in AMIP_TROP exhibits the trough-to-ridge transition as in observations (not shown). These results indicate that the wet-to-dry transition in AMIP_TROP does not arise from coincidence. The strong and persistent MJO convection in the western Pacific was an active driver for the transition from wet/trough to dry/ridge conditions over California in early 2013.

4. Results From Seasonal and Subseasonal Multi-Model Ensemble System

4.1. On the Role of SST Anomalies Before the Transition

This section explores why the seasonal prediction models failed to predict the wet-to-dry transition (Figure 1a), based on the findings of Section 3. First, we examine the SST prediction for December 2012 in the NMME models (Table 2) since we find a role for SST anomalies in driving wet/trough conditions in early winter in AMIP (Figure 3). Figures 7b and 7c show the multi-model ensemble-mean (MME) SST and Z200 anomalies of December 2012 simulated in nine NMME models, which are initialized in October and November 2012. Each forecast thus represents a 2.5-month and 1.5-month forecast lead time, respectively. For example, when the model is initialized on November 15, 2012 and the forecast is

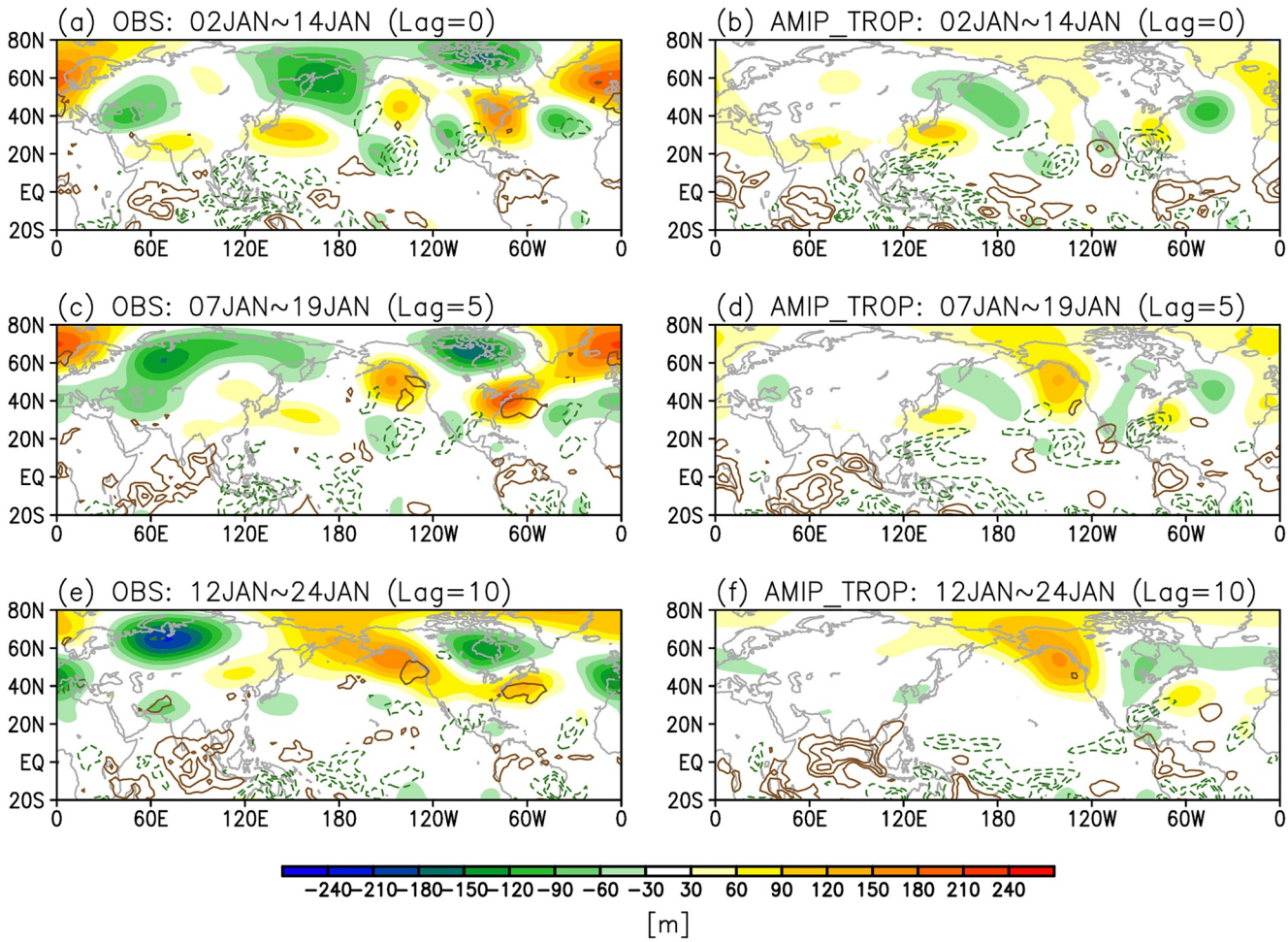

Figure 6. (a) Composite of 20–100 days filtered Z200 (shading) and Outgoing Longwave Radiation (OLR) (contour) anomalies for January 2–14 in observations. (c), (e) Same as (a) but Z200 at lag 5 (January 7–19) and lag 10 (January 12–24). (b, d, f) Same as (a, c, e) but in AMIP_TROP. The contour interval of OLR is 12 W m^{-2}, and zero contours are omitted.

run until the end of December, it is defined as a 1.5-month forecast lead-time (Kirtman et al., 2014). We show the MME of the nine NMME models to discuss the general skill of the NMME forecasts for this particular event.

Figure 7a shows the observed SST and Z200 anomalies in December 2012, with the tropical-extratropical wave train and trough in the ENP domain that has been discussed in Section 3. The NMME forecasts initialized in October and November fail to predict the ENP trough and instead predict a weakened Aleutian low and anticyclonic conditions in the ENP domain (Figures 7b, 7c, and S7b), resulting in a prediction of neutral or slightly dry conditions in December over California (Figures 1a and S7a). A closer look at individual model forecasts reveals that none of the nine NMME models predicted the ENP trough when initialized in October (Figures S7b and S8). All NMME models underestimate the warm SST anomaly in the South China Sea and rather exhibit warm SST anomalies in the central Indian Ocean and central or eastern Pacific Ocean. The spatial correlations between tropical Pacific SST anomalies in the model and observations are under 0.5. Thus, it is not surprising that these forecasts show no skill in predicting the tropical-extratropical teleconnection.

Although the general prediction skill of tropical SST is quite high, with anomaly correlations of 0.5 or higher even in 5-month lead forecasts (Becker et al., 2020), it does not show up in this specific year. Several reasons may explain the poor performance in predicting the 2012/13 tropical SST. First, the SST anomalies in 2012/13 winter were weak, and a weak signal is harder to predict (Hoskins, 2013). Second, initial errors

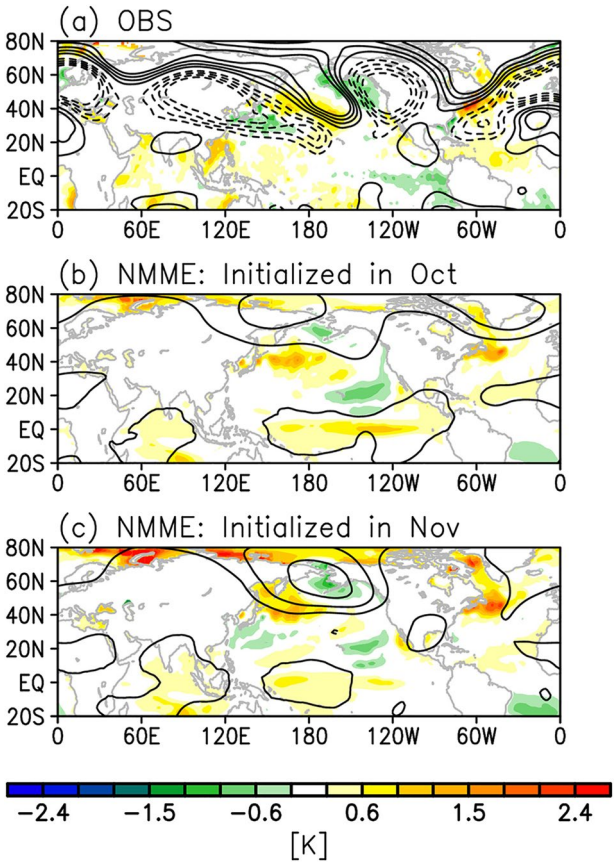

Figure 7. (a) SST (shading) and Z200 anomalies (contours) in December 2012 from observations. (b)–(c) Same as (a) but for the multi-model mean of North American Multi-Model Ensemble (NMME) models, initialized in (b) October and (c) November. The contour interval of Z200 is 20 m, and zero contours are omitted.

in the tropics may have led to a failed prediction of SST. For instance, Hua and Su (2020) found that the initial cold errors in the southeastern Pacific Ocean lead to the failed prediction of El Niño events in the NMME models, disturbing the development of warm SST anomalies in the eastern Pacific. The impact of initial errors that grow rapidly is also suggested in Newman and Sardeshmukh (2017). A similar problem is found in this case study. Figure 8 shows the relationship between initialized SST (i.e., 0.5-month lead time) and December forecasted SST using the NMME forecasts initialized in October and November. It is examined in the South China Sea (90°–120°E, 0°–20°N; Figure 8a) and in the eastern Pacific Ocean (150°–70°W, 10°S–10°N; Figure 8b) where warm and cool SST anomalies are shown in December, respectively (Figure 7a). NCAR-CCSM3, NCAR-CCSM4, and NASA-GMAO-GEOS5 have the largest initial warm error in the eastern Pacific, and GFDL-CM2p1-aer04 shows the largest initial cold error in the western Pacific. The observed SST anomalies change from normal to warm (cool) in the South China Sea (eastern Pacific Ocean), whereas all NMME models tend to maintain their initial states, close to the one-to-one line (gray dotted line in Figure 8). The initial model errors persist throughout the forecast period, and even models with an accurate SST at initialization do not capture the observed evolution of SST anomalies (e.g., ECCC-GEM-NEMO in Figure 8b). Reducing initial error in tropical SST and improving the prediction of its temporal evolution will improve the overall usefulness of NMME model predictions.

4.2. On the Role of the MJO in Triggering the Transition

To examine the MJO impacts on the prediction of the wet-to-dry transition in January, 12 subseasonal prediction models (Table 3; Section 2.4) are used (recall NMME daily data is not available for the 2012/13 winter). Figure S9 shows the composite of OLR and Z200 anomalies in each of the 12 subseasonal prediction models. We examine whether the prediction of MJO activity in January influences the prediction of dry/ridge conditions. In Figure 9, we compare a good (UKMO-GloSea5) and a poor (GMAO-GEOS) week-2 prediction to observations. The OLR anomalies

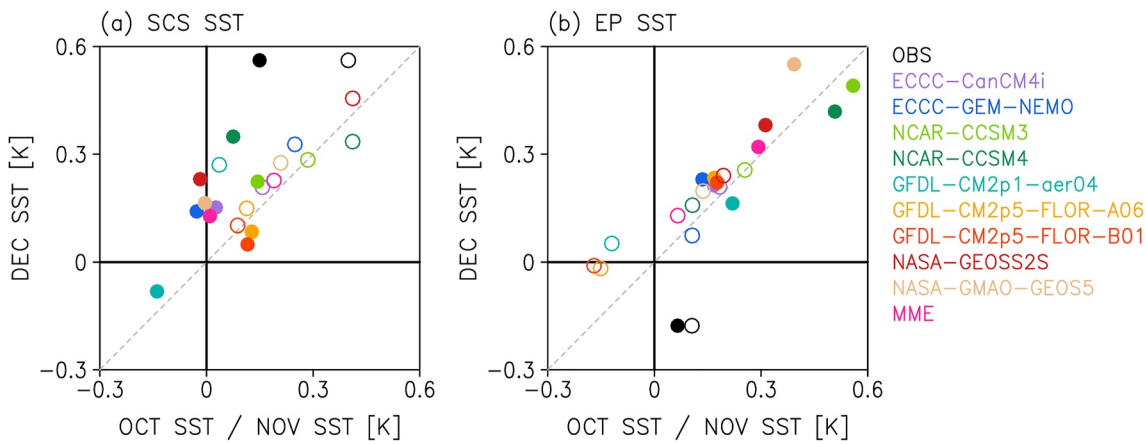

Figure 8. (a) Relationship of South China Sea (SCS; 90°–120°E, 0°–20°N) SST anomalies between the initial value and the predicted value for December 2012. The closed circle and opened circle denote the values initialized in October and November, respectively. For example, the initial value of closed circles is the predicted value in October 2012, and the initial value of opened circles is in November 2012. Different colors indicate individual North American Multi-Model Ensemble (NMME) models, observations are in black. (b) Same with (a) but using the eastern Pacific SST (EP; 90°–120°E, 0°–20°N).

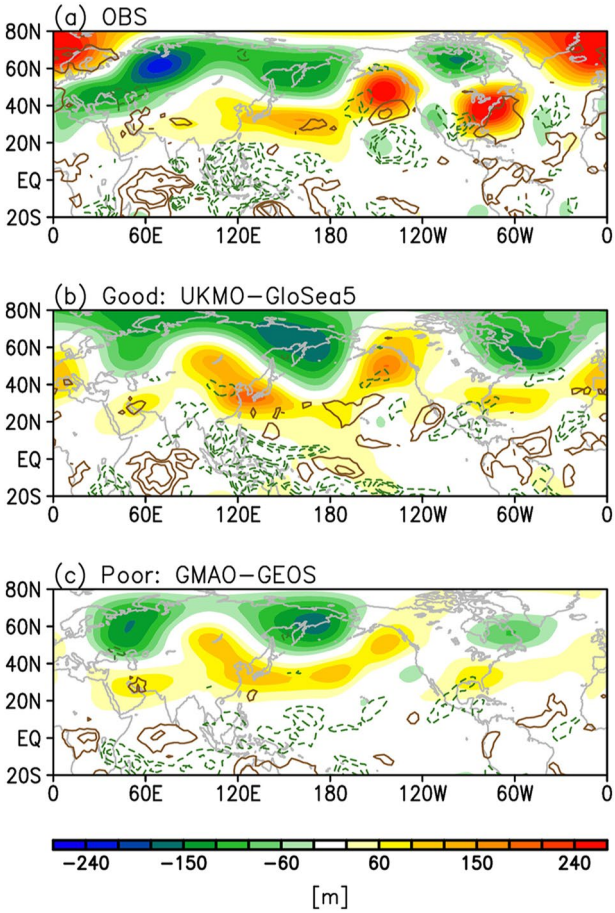

Figure 9. Composite of Z200 (shading) and Outgoing Longwave Radiation (OLR) (contour) anomalies in (a) observations, (b) good prediction, and (c) poor prediction among the week-2 predictions of 12 subseasonal prediction models. Note that the previous 120-day averaged values are also excluded in each variable. The OLR anomalies are averaged for January 2–14, and Z200 anomalies are averaged for January 7–19. The green contours denote the values at −36, −24, and −12 W m^{-2}, indicating the enhanced convection. The OLR anomalies at 12, 24, and 36 W m^{-2} are contoured in brown, indicating the suppressed convection.

are averaged for January 2–14, and the Z200 anomalies are averaged for January 7–19 (including a 5-day time lag; see Figure 6). Since the time filtering is unavailable in the forecast data, the previous 120-day averaged data are subtracted from the anomaly data to isolate the MJO-related signal (e.g., Gottschalck et al., 2010; Lim et al., 2018). For example, the previous 120-day averaged data of the day-1 forecast are calculated based on the previous 119 days of the observations and the first day of reforecasts. Following Pegion et al. (2019), reforecasts that are produced during the prior week (previous Friday–Thursday) are defined as the week-1 prediction. For instance, the week-1 prediction in this study indicates the reforecasts initialized on December 28 to January 3 when it is before 1 week from the first occurrence of the MJO phases 4 and 5 (i.e., January 2). The week-2, week-3, and week-4 predictions are initialized for December 21–27, 14–20, and 7–13, respectively.

In models that capture the strong enhanced convection in the western Pacific, the strong ENP ridge is well predicted (i.e., BoM-POAMA, CMA-BCC in Figure S9, UKMO-GloSea5 in Figure 9b). The MJO convection in these models is well organized at the initial time and propagates eastward for 3 weeks (not shown). In contrast, the opposite is found in the models with a weak MJO convection (i.e., CESM-30LCESM1, CESM-46LCESM1, and ECCC-GEPS in Figure S9, GMAO-GEOS in Figure 9c). In these models, the MJO convection is rapidly disorganized at week-2. The small amplitude in the MJO convection prevents a strong teleconnection in the extratropics from happening, causing only a weak ENP ridge anomaly. This result highlights how a good prediction of the MJO can benefit CA rainfall prediction at the subseasonal time scale.

This relationship between MJO convection and ENP ridge is robust in the week-1 to week-4 forecasts (Figure 10a). Here, the MJO convection is defined by the OLR averaged over the western Pacific (WP_OLR; 110°–140°E, 15°S–10°N) for January 2–14. The ENP ridge is determined by the area-averaged Z200 in the eastern North Pacific (ENP_Z200; 150°–110°W, 30°–55°N) for January 7–19. The direct relationship between MJO convection and CA precipitation is also evaluated in Figure 10b. It is evident from Figures 10a and 10b that the prediction of western Pacific MJO convection is linked to the prediction of dry/ridge conditions in California, with negative correlation between ENP_Z200 and WP_OLR and positive correlation between CA precipitation and WP_OLR. For example, the week-2 prediction of UKMO-GloSea5, which shows the strongest MJO convection, predicts the second strongest ENP ridge (Figure 10a) and CA dry conditions (Figure 10b). The week-4 prediction of UKMO-GloSea5, which shows the weakest convection, predicts an ENP trough and excess of rain over California. These results further demonstrate that the MJO convection was a driver for the transition toward dry conditions over California in January via the tropical-extratropical teleconnection.

These relationships continuously increase when the week 3–4 forecasts are considered (gold colored numbers in Figure 10), compared to using the week 1–4 forecasts (navy colored numbers in Figure 10). Considering that the relationship between WP_OLR and ENP_Z200 remains strong (−0.6 correlation) regardless of the forecast lead time (Figure 10c), this result emphasizes that improvement of MJO prediction may benefit the CA precipitation prediction beyond the 2-week time scale. Dias and Kiladis (2019) showed that the extratropical prediction skill in week 2–4 forecasts is dependent on the tropical prediction skill in subseasonal prediction models. Likewise, Jung et al. (2010) showed that the midlatitude prediction could be improved after nudging the tropics. Our results are consistent with these previous studies.

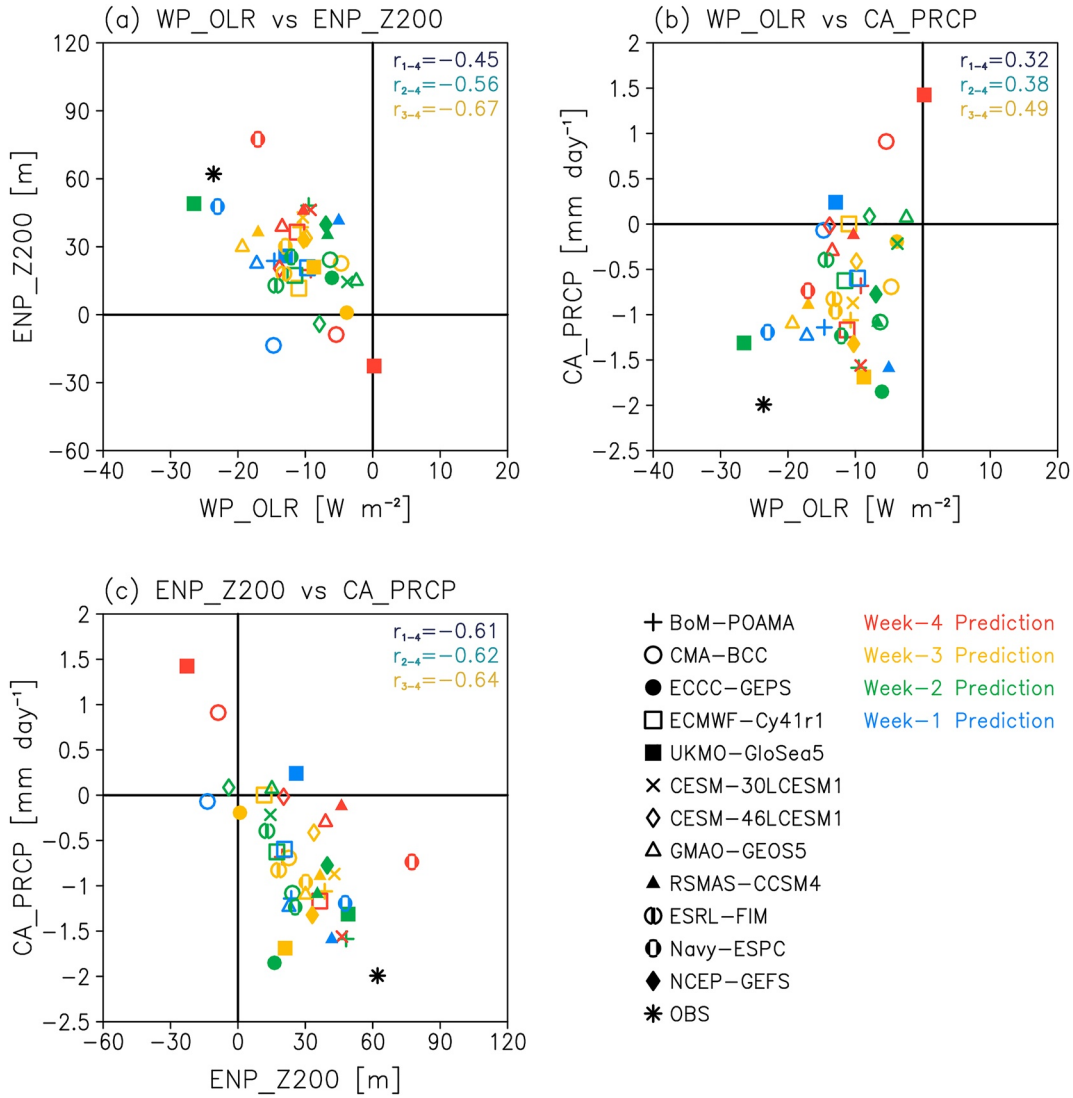

Figure 10. (a) Relationship between western Pacific (WP; 110°–140°E, 15°S–10°N) Outgoing Longwave Radiation (OLR) anomalies for January 2–14 and eastern North Pacific (ENP; 150°–110°W, 30°–55°N) Z200 for January 7–9. (b) Relationship between WP OLR and California (CA) precipitation (CA PRCP) for January 7–19. (c) Relationship between ENP Z200 and CA PRCP. Note that the previous 120-day averaged values are excluded in each variable. Different marks denote the different models and the observations. Blue, green, yellow, and red marks denote the week-1, week-2, week-3, and week-4 predictions, respectively. The r_{1-4} in the top right corner indicates the correlation coefficient of each relationship using week 1–4 predictions, and r_{2-4} and r_{3-4} are calculated by using week 2–4 and week 3–4 predictions, respectively.

5. Summary and Discussion

Using a combination of model experiments and forecasts, we demonstrate that the observed wet-to-dry transition of CA rainfall during the 2012/13 winter was mainly the result of the combined effects of tropical SST and strong MJO activity. In our AMIP experiments, we find that the tropical SST has an impact on the wet/trough conditions in November–December 2012, while the regime change to dry/ridge conditions in January 2013 is driven by the MJO teleconnection when tropical variability is imposed in the model. The role for the MJO is supported by evidence from the subseasonal prediction models, making January 2013 an example of "window of opportunity" for S2S prediction of CA rainfall. The NMME seasonal prediction models, however, have difficulty in predicting not only the wet-to-dry transition of CA precipitation but also the tropical SST (Figure 7), which is found as a driver for wet/trough conditions in California (Figure 3).

Although the exact role of SST in triggering the tropical-extratropical teleconnection is unknown, this case study illustrates how improvement in tropical SST prediction (especially in the absence of a strong ENSO) is needed to achieve a higher forecast skill in the extratropics. Our experiments with nudging the Arctic suggest a secondary role for high-latitude atmospheric variability when compared to the influence of the tropics. Still, it helps shape the midlatitude response to the tropical forcing and reduces the spread among ensemble members. Therefore, improving predictions of the high-latitude processes at the S2S time scales would probably also benefit S2S predictions of midlatitude variability and CA rainfall.

Although this study identifies the MJO as a driver of the wet-to-dry transition, we did not investigate why dry conditions persisted throughout February and March 2013. Interestingly, AMIP_TROP and AMIP_TRHL partly simulate a persistence in the ridge (Figures 5b, S2e, S2g, S3e, and S3g) in February and March. However, although quite active, the influence of MJO is not clearly shown in February and March, and how much S2S predictability may have been levered during this event is unclear. A potential driver may have been the sudden stratospheric warming that happened in early 2013, but it did not persist beyond mid-January. It is difficult to imagine how it may have impacted the ridge in February-March. It would be interesting to explore why AMIP_TROP and AMIP_TRHL simulate the persistence of the ridge in future work.

An interesting finding of this study is that the MJO activity partly explains the drought of 2012/13 winter when previous studies considered it to be driven by internal variability (Wang & Schubert, 2014). This supports the idea that unpredictable internal atmospheric variability at the seasonal time scale can be a predictable signal at the subseasonal time scale (Robertson et al., 2020; Wang et al., 2017). Of course, the present study has been limited to exploring potential mechanisms for CA rainfall variability of one winter season only. Applying this approach to other transition cases, such as the normal-to-dry transition of 2015/16 (Jong et al., 2018), or the other recent drought years of 2012–2016 which have been understood as primarily impacted by internal variability (Seager et al., 2015; Watson et al., 2016), may help identify potential mechanisms that could be useful to the S2S and larger-range forecasting effort.

Data Availability Statement

The sources of data used in this study are as follows. MERRA-2 reanalysis data were obtained from http://goldsmr5.gesdisc.eosdis.nasa.gov/data/MERRA2/. NOAA OLR data were from https://psl.noaa.gov/data/gridded/data.interp_OLR.html, and OMI for MJO index was from https://psl.noaa.gov/mjo/mjoindex/omi.1x.txt. The CPC US Unified Precipitation data were downloaded from https://psl.noaa.gov/data/gridded/data.unified.daily.conus.html, and HadISST1 was from https://www.metoffice.gov.uk/hadobs/hadisst/data/download.html. NMME data set was available in https://iridl.ldeo.columbia.edu/SOURCES/.Models/.NMME/. CESM1 models and SubX models were obtained from https://iridl.ldeo.columbia.edu/SOURCES/.Models/.SubX/, and S2S models were from https://iridl.ldeo.columbia.edu/SOURCES/.ECMWF/.S2S/. The model output from AMIP experiments was published at this site (https://doi.org/10.5281/zenodo.5606152).

Acknowledgments
This study was supported by the Department of Water Resources (Contract number: 4600013127). The authors are grateful to the time and expertise of anonymous reviewers. The authors acknowledge the NOAA, NASA, and IRI for providing the data set.

References

Adler, R. F., Huffman, G. J., Chang, A., Ferraro, R., Xie, P.-P., Janowiak, J., et al. (2003). The Version 2 Global Precipitation Climatology Project (GPCP) monthly precipitation analysis (1979-Present). *Journal of Hydrometeorology*, *4*, 1147–1167. https://doi.org/10.1175/1525-7541(2003)004<1147:tvgpcp>2.0.co;2

Baldwin, M. P., Ayarzagüena, B., Birner, T., Butchart, N., Butler, A. H., Charlton-Perez, A. J., et al. (2021). Sudden stratospheric warmings. *Reviews of Geophysics*, *59*, e2020RG000708. https://doi.org/10.1029/2020RG000708

Barnston, A. G., Tippett, M. K., van den Dool, H. M., & Unger, D. A. (2015). Toward an improved multimodel ENSO prediction. *Journal of Applied Meteorology and Climatology*, *54*, 1579–1595. https://doi.org/10.1175/JAMC-D-14-0188.1

Barsugli, J. J., & Sardeshmukh, P. D. (2002). Global atmospheric sensitivity to tropical SST anomalies throughout the Indo-Pacific basin. *Journal of Climate*, *15*, 3427–3442. https://doi.org/10.1175/1520-0442(2002)015<3427:gastts>2.0.co;2

Becker, E. J., Berbery, E. H., & Higgins, R. W. (2011). Modulation of cold-season U.S. daily precipitation by the Madden–Julian oscillation. *Journal of Climate*, *24*, 5157–5166. https://doi.org/10.1175/2011JCLI4018.1

Becker, E. J., Kirtman, B. P., & Pegion, K. (2020). Evolution of the North American multi-model ensemble. *Geophysical Research Letters*, *47*, e2020GL087408. https://doi.org/10.1029/2020GL087408

Cohen, J., Pfeiffer, K., & Francis, J. (2017). Winter 2015/16: A turning point in ENSO-based seasonal forecasts. *Oceanography*, *30*(1), 82–89. https://doi.org/10.5670/oceanog.2017.115

Cooper, M. G., Schaperow, J. R., Cooley, S. W., Alam, S., Smith, L. C., & Lettenmaier, D. P. (2018). Climate elasticity of low flows in the maritime western U.S. Mountains. *Water Resources Research*, *54*, 5602–5619. https://doi.org/10.1029/2018WR022816

Dias, J., & Kiladis, G. N. (2019). The influence of tropical forecast errors on higher latitude predictions. *Geophysical Research Letters*, *46*, 4450–4459. https://doi.org/10.1029/2019GL082812

Frankson, R., Stevens, L., Kunkel, K., Champion, S., Easterling, D. & Sweet, W. (2017). *California State Climate Summary (NOAA Technical Report NESDIS 149-CA, p. 4)*. https://statesummaries.ncics.org/chapter/ca/

Gelaro, R., McCarty, W., Suarez, M. J., Todling, R., Molod, A., Takacs, L., et al. (2017). The Modern-Era Retrospective Analysis for Research and Applications, Version 2 (MERRA-2). *Journal of Climate*, *30*, 5419–5454. https://doi.org/10.1175/JCLI-D-16-0758.1

Gottschalck, J., Wheeler, M., Weickmann, K., Vitart, F., Savage, N., Lin, H., et al. (2010). A framework for assessing operational Madden–Julian oscillation forecasts: A CLIVAR MJO Working Group project. *Bulletin of the American Meteorological Society*, *91*, 1247–1258. https://doi.org/10.1175/2010BAMS2816.1

Guirguis, K., Gershunov, A., Shulgina, T., Clemesha, R. E. S., & Ralph, F. M. (2019). Atmospheric rivers impacting Northern California and their modulation by a variable climate. *Climate Dynamics*, *52*, 6569–6583. https://doi.org/10.1007/s00382-018-4532-5

Hartmann, D. L. (2015). Pacific sea surface temperature and the winter of 2014. *Geophysical Research Letters*, *42*, 1894–1902. https://doi.org/10.1002/2015GL063083

Hoskins, B. (2013). The potential for skill across the range of the seamless weather-climate prediction problem: A stimulus for our science. *Quarterly Journal of the Royal Meteorological Society*, *139*, 573–584. https://doi.org/10.1002/qj.1991

Hoskins, B. J., & Karoly, D. (1981). The steady linear response of a spherical atmosphere to thermal and orographic forcing . *Journal of the Atmospheric Sciences*, *38*, 1179–1196. https://doi.org/10.1175/1520-0469(1981)038<1179:tslroa>2.0.co;2

Hua, L., & Su, J. (2020). Southeastern Pacific error leads to failed El Niño forecasts. *Geophysical Research Letters*, *47*, e2020GL088764. https://doi.org/10.1029/2020GL088764

Hurrell, J. W., Hack, J. J., Shea, D., Caron, J. M., & Rosinski, J. (2008). A new sea surface temperature and sea ice boundary dataset for the Community Atmosphere Model. *Journal of Climate*, *21*, 5145–5153. https://doi.org/10.1175/2008JCLI2292.1

Jong, B.-T., Ting, M., Seager, R., Henderson, N., & Lee, D. E. (2018). Role of equatorial Pacific SST forecast error in the late winter California precipitation forecast for the 2015/16 El Niño. *Journal of Climate*, *31*, 839–852. https://doi.org/10.1175/JCLI-D-17-0145.1

Jung, T., Miller, M. J., & Palmer, T. N. (2010). Diagnosing the origin of extended-range forecast errors. *Monthly Weather Review*, *138*(6), 2434–2446. https://doi.org/10.1175/2010mwr3255.1

Kiladis, G. N., Dias, J., Straub, K. H., Wheeler, M. C., Tulich, S. N., Kikuchi, K., et al. (2014). A comparison of OLR and circulation-based indices for tracking the MJO. *Monthly Weather Review*, *142*(5), 1697–1715. https://doi.org/10.1175/MWR-D-13-00301.1

Kirtman, B. P., Min, D., Infanti, J. M., Kinter, J. L., III, Paolino, D. A., Zhang, Q., et al. (2014). The North American Multimodel Ensemble: Phase-1 seasonal-to-interannual prediction; Phase-2 toward developing intraseasonal prediction. *Bulletin of the American Meteorological Society*, *95*, 585–601. https://doi.org/10.1175/BAMS-D-12-00050.1

Knowles, N., Dettinger, M. D., & Cayan, D. R. (2006). Trends in snowfall versus rainfall in the western United States. *Journal of Climate*, *19*, 4545–4559. https://doi.org/10.1175/jcli3850.1

Kumar, A., & Chen, M. (2020). Understanding skill of seasonal mean precipitation prediction over California during boreal winter and role of predictability limits. *Journal of Climate*, *33*, 6141–6163. https://doi.org/10.1175/JCLI-D-19-0275.1

Lau, N. C., & Nath, M. J. (1994). A modeling study of the relative roles of tropical and extratropical SST anomalies in the variability of the global atmosphere-ocean system. *Journal of Climate*, *7*, 1184–1207. https://doi.org/10.1175/1520-0442(1994)007<1184:AMSOTR>2.0.CO;2

Lee, M.-Y., Hong, C.-C., & Hsu, H.-H. (2015). Compounding effects of warm sea surface temperature and reduced sea ice on the extreme circulation over the extratropical North Pacific and North America during the 2013–2014 boreal winter. *Geophysical Research Letters*, *42*, 1612–1618. https://doi.org/10.1002/2014GL062956

Lee, S.-K., Lopez, H., Chung, E.-S., DiNezio, P., Yeh, S.-W., & Wittenberg, A. T. (2018). On the fragile relationship between El Niño and California rainfall. *Geophysical Research Letters*, *45*, 907–915. https://doi.org/10.1002/2017GL076197

Li, W., & Forest, C. E. (2014). Estimating the sensitivity of the atmospheric teleconnection patterns to SST anomalies using a linear statistical method. *Journal of Climate*, *27*, 9065–9081. https://doi.org/10.1175/JCLI-D-14-00231.1

Liebmann, B., & Smith, C. A. (1996). Description of a complete (interpolated) outgoing longwave radiation dataset. *Bulletin of the American Meteorological Society*, *77*, 1275–1277. http://www.jstor.org/stable/26233278

Lim, Y., Son, S.-W., & Kim, D. (2018). MJO prediction skill of the subseasonal-to-seasonal prediction models. *Journal of Climate*, *31*, 4075–4094. https://doi.org/10.1175/JCLI-D-17-0545.1

Lund, J., Medellin-Azuara, J., Durand, J., & Stone, K. (2018). Lessons from California's 2012-2016 Drought. *Journal of Water Resources Planning and Management*, *144*, 04018067. https://doi.org/10.1061/(asce)wr.1943-5452.0000984

Madden, R. A., & Julian, P. R. (1971). Detection of a 40–50 day oscillation in the zonal wind in the tropical pacific. *Journal of the Atmospheric Sciences*, *28*, 702–708. https://doi.org/10.1175/1520-0469(1971)028<0702:DOADOI>2.0.CO;2

Mo, K. C., & Higgins, W. R. (1998). Tropical convection and precipitation regimes in the western United States. *Journal of Climate*, *11*, 2404–2423. https://doi.org/10.1175/1520-0442(1998)011<2404:TCAPRI>2.0.CO;2

Newman, M., & Sardeshmukh, P. D. (1998). The impact of the annual cycle on the North Pacific/North American response to remote low-frequency forcing. *Journal of the Atmospheric Sciences*, *55*, 1336–1353. https://doi.org/10.1175/1520-0469(1998)055<1336:tiotac>2.0.co;2

Newman, M., & Sardeshmukh, P. D. (2017). Are we near the predictability limit of tropical Indo-Pacific sea surface temperatures? *Geophysical Research Letters*, *44*, 8520–8529. https://doi.org/10.1002/2017GL074088

Paek, H., Yu, J.-Y., & Qian, C. (2017). Why were the 2015/2016 and 1997/1998 extreme El Niños different? *Geophysical Research Letters*, *44*, 1848–1856. https://doi.org/10.1002/2016GL071515

Pegion, K., Kirtman, B. P., Becker, E., Collins, D. C., LaJoie, E., Burgman, R., et al. (2019). The Subseasonal Experiment (SubX): A multimodel subseasonal prediction experiment. *Bulletin of the American Meteorological Society*, *100*, 2043–2060. https://doi.org/10.1175/BAMS-D-18-0270.1

Rayner, N. A., Parker, D. E., Horton, E. B., Folland, C. K., Alexander, L. V., Rowell, D. P., et al. (2003). Global analyses of sea surface temperature, sea ice, and night marine air temperature since the late nineteenth century. *Journal of Geophysical Research: Atmospheres*, *108*, 4407. https://doi.org/10.1029/2002JD002670

Robertson, A. W., Vigaud, N., Yuan, J., & Tippett, M. K. (2020). Toward identifying subseasonal forecasts of opportunity using North American weather regimes. *Monthly Weather Review*, *148*, 1861–1875. https://doi.org/10.1175/MWR-D-19-0285.1

Ropelewski, C. F., & Halpert, M. S. (1986). North American precipitation and temperature patterns associated with the El Niño/Southern Oscillation (ENSO). *Monthly Weather Review*, *114*, 2352–2362. https://doi.org/10.1175/1520-0493(1986)114<2352:NAPATP>2.0.CO;2

Sardeshmukh, P. D., & Hoskins, B. J. (1988). The generation of global rotational flow by steady idealized tropical divergence. *Journal of the Atmospheric Sciences*, *45*, 1228–1251. https://doi.org/10.1175/1520-0469(1988)045<1228:TGOGRF>2.0.CO;2

Seager, R., & Henderson, N. (2016). On the role of tropical ocean forcing of the persistent North American West Coast Ridge of Winter 2013/14. *Journal of Climate*, *29*, 8027–8049. https://doi.org/10.1175/JCLI-D-16-0145.1

Seager, R., Hoerling, M., Schubert, S., Wang, H., Lyon, B., Kumar, A., et al. (2015). Causes of the 2011-14 California drought. *Journal of Climate*, *28*, 6997–7024. https://doi.org/10.1175/JCLI-D-14-00860.1

Seager, R., & Hoerling, M. (2014). Atmosphere and ocean origins of North American droughts. *Journal of Climate*, *27*, 4581–4606. https://doi.org/10.1175/JCLI-D-13-00329.1

Singh, D., Ting, M., Scaife, A. A., & Martin, N. (2018). California winter precipitation predictability: Insights from the anomalous 2015–2016 and 2016–2017 seasons. *Geophysical Research Letters*, *45*, 9972–9980. https://doi.org/10.1029/2018GL078844

Slater, L. J., Villarini, G., & Bradley, A. A. (2019). Evaluation of the skill of North-American Multi-Model Ensemble (NMME) Global Climate Models in predicting average and extreme precipitation and temperature over the continental USA. *Climate Dynamics*, *53*, 7381–7396. https://doi.org/10.1007/s00382-016-3286-1

Smith, K. L., Neely, R. R., Marsh, D. R., & Polvani, L. M. (2014). The Specified Chemistry Whole Atmosphere Community Climate Model (SC-WACCM). *Journal of Advances in Modeling Earth Systems*, *6*, 883–901. https://doi.org/10.1002/2014MS000346

Swain, D. L., Horton, D. E., Singh, D., & Diffenbaugh, N. S. (2016). Trends in atmospheric patterns conducive to seasonal precipitation and temperature extremes in California. *Science Advances*, *2*, e1501344. https://doi.org/10.1126/sciadv.1501344

Swain, D. L., Singh, D., Horton, D. E., Mankin, J. S., Ballard, T. C., & Diffenbaugh, N. S. (2017). Remote linkages to anomalous winter atmospheric ridging over the northeastern Pacific. *Journal of Geophysical Research: Atmospheres*, *122*(12), 12,194–12,209. https://doi.org/10.1002/2017JD026575

Swain, D. L., Tsiang, M., Haugen, M., Singh, D., Charland, A., Rajaratnam, B., & Diffenbaugh, N. (2014). The extraordinary California drought of 2013/2014: Character, context, and the role of climate change [in "Explaining Extremes of 2013 from a Climate Perspective"]. *Bulletin of the American Meteorological Society*, *95*(9), S3–S7. https://doi.org/10.1175/1520-0477-95.9.S1.1

Teng, H., & Branstator, G. (2017). Causes of extreme ridges that induce California droughts. *Journal of Climate*, *30*, 1477–1492. https://doi.org/10.1175/JCLI-D-16-0524.1

U.S. Census Bureau. (2019). *QuickFacts California*. Retrieved from https://www.census.gov/quickfacts/fact/table/CA/PST045219

U.S. Department of Agriculture. (2020). *California Agricultural Statistics Review 2018-2019*. Retrieved from https://www.cdfa.ca.gov/statistics/PDFs/2018-2019AgReportnass.pdf

Vitart, F., Ardilouze, C., Bonet, A., Brookshaw, A., Chen, M., Codorean, C., et al. (2017). The Sub-seasonal to Seasonal (S2S) prediction project database. *Bulletin of the American Meteorological Society*, *98*, 163–173. https://doi.org/10.1175/BAMS-D-16-0017.1

Wang, H., & Schubert, S. (2014). Causes of the extreme dry conditions over California during early 2013 [in "Explaining Extremes of 2013 from a Climate Perspective"]. *Bulletin of the American Meteorological Society*, *95*(9), S7–S11. https://doi.org/10.1175/1520-0477-95.9.S1.1

Wang, S.-Y., Anichowski, A., Tippett, M. K., & Sobel, A. H. (2017). Seasonal noise versus subseasonal signal: Forecasts of California precipitation during the unusual winters of 2015–2016 and 2016–2017. *Geophysical Research Letters*, *44*, 9513–9520. https://doi.org/10.1002/2017GL075052

Wang, S.-Y., Hipps, L., Gillies, R. R., & Yoon, J.-H. (2014). Probable causes of the abnormal ridge accompanying the 2013–2014 California drought: ENSO precursor and anthropogenic warming footprint. *Geophysical Research Letters*, *41*, 3220–3226. https://doi.org/10.1002/2014GL059748

Watson, P. A. G., Weisheimer, A., Knight, J. R., & Palmer, T. N. (2016). The role of the tropical West Pacific in the extreme Northern Hemisphere winter of 2013/2014. *Journal of Geophysical Research: Atmospheres*, *121*, 1698–1714. https://doi.org/10.1002/2015JD024048

Xu, F., & San Liang, X. (2017). On the generation and maintenance of the 2012/13 sudden stratospheric warming. *Journal of the Atmospheric Sciences*, *74*, 3209–3228. https://doi.org/10.1175/JAS-D-17-0002.1